

# High-temperature field-free superconducting diode effect in high- $T_c$ cuprates

Received: 10 July 2024

Accepted: 3 January 2025

Published online: 09 January 2025

Shichao Qi<sup>1,7</sup>, Jun Ge<sup>1,7</sup>, Chengcheng Ji<sup>1,2,7</sup>, Yiwen Ai<sup>1</sup>, Gaoxing Ma<sup>1</sup>, Ziqiao Wang<sup>1</sup>, Zihan Cui<sup>3</sup>, Yi Liu<sup>3,4</sup>, Ziqiang Wang<sup>5</sup> & Jian Wang<sup>1,2,6</sup>✉

The superconducting diode effect (SDE) is defined by the difference in the magnitude of critical currents applied in opposite directions. It has been observed in various superconducting systems and attracted high research interests. However, the operating temperature of the SDE is typically low and/or the sample structure is rather complex. For the potential applications in non-dissipative electronics, efficient superconducting diodes working in zero magnetic field with high operating temperatures and a simple configuration are highly desired. Here, we report the observation of a SDE under zero magnetic field with operating temperatures up to 72 K and efficiency as high as 22% at 53 K in high-transition-temperature (high- $T_c$ ) cuprate superconductor  $\text{Bi}_2\text{Sr}_2\text{CaCu}_2\text{O}_{8+\delta}$  (BSCCO) flake devices. The rectification effect persists beyond two hundred sweeping cycles, confirming the stability of the superconducting diode. Our results offer promising developments for potential applications in non-dissipative electronics, and provide insights into the mechanism of field-free SDE and symmetry breakings in high- $T_c$  superconductors.

Nonreciprocal charge transport<sup>1–5</sup>, arising from the symmetry-breaking properties of materials, describes the asymmetric behavior of voltage with currents flowing in opposite directions. One typical example of nonreciprocity is the p-n junction in semiconductors, where the inversion symmetry is naturally broken due to the imbalance of chemical potential distribution<sup>6</sup>. When the electric current flows through such a semiconductor diode, the resistance is small in one direction but becomes dramatically large in the opposite direction, giving rise to the half-wave rectification effect. The stable half-wave rectification effect enables the semiconductor diode to serve as a fundamental component in electronic circuits. However, the unavoidable Joule heating in the semiconductor diode increases the energy consumption and impedes further integration of the circuit.

One practical approach to achieve low power consumption in electronic circuits is to utilize the superconducting diode<sup>7–12</sup>, whose critical current in one direction (positive) is different in magnitude from that in the opposite (negative) direction. As a unidirectional current with amplitude in between the two disparate critical currents is applied, the superconducting diode remains in the zero-resistance state in one direction and becomes resistive when the current direction is reversed. In general, the emergence of the superconducting diode effect (SDE) requires simultaneous breaking of inversion symmetry and time-reversal symmetry (TRS)<sup>13–17</sup>. Up to now, the SDE has been observed in various non-centrosymmetric superlattices<sup>8</sup>, Josephson junctions<sup>18–23</sup>, nano-fabricated devices<sup>24–29</sup>, and films<sup>30–32</sup> under magnetic field. The inversion symmetry breaking can arise from

<sup>1</sup>International Center for Quantum Materials, School of Physics, Peking University, Beijing, China. <sup>2</sup>Hefei National Laboratory, Hefei, China. <sup>3</sup>Department of Physics and Beijing Key Laboratory of Opto-electronic Functional Materials & Micro-nano Devices, Renmin University of China, Beijing, China. <sup>4</sup>Key Laboratory of Quantum State Construction and Manipulation (Ministry of Education), Renmin University of China, Beijing, China. <sup>5</sup>Department of Physics, Boston College, Chestnut Hill, MA, USA. <sup>6</sup>Collaborative Innovation Center of Quantum Matter, Beijing, China. <sup>7</sup>These authors contributed equally: Shichao Qi, Jun Ge, Chengcheng Ji. ✉e-mail: [jianwangphysics@pku.edu.cn](mailto:jianwangphysics@pku.edu.cn)

the asymmetry of stacked heterostructure<sup>8,19</sup>, crystal lattice<sup>24,25,27</sup>, artificial device configuration<sup>23,30</sup>, device edge<sup>21,29,31</sup> and interface<sup>22</sup>, while broken TRS is usually achieved by applying an external magnetic field. Intriguingly, the zero-field SDE is reported in some superconducting systems<sup>33–42</sup> where the TRS breaking arises from the ferromagnetism of the magnetic layers<sup>33,36,37</sup>, valley polarization<sup>43,44</sup>, self-field effect, and stray fields from trapped Abrikosov vortices<sup>35</sup>, interface magnetism<sup>40</sup>, current induced reduction of degeneracy<sup>41</sup> and dynamic superconducting domains<sup>42</sup>. However, the operating temperature of these superconducting diodes<sup>8,18–20,23–40,42</sup> is relatively low, and/or the structure of the diode devices is rather complex<sup>21,22,41</sup>, which impede its implementation in the circuit. Field-free high-temperature superconducting diode with significant efficiency in a simple structure is highly desired for exploring potential applications in low-power-consumption electronics, as well as for probing the time-reversal and inversion symmetry breakings in unconventional superconductors.

Here, we report the observation of field-free high-temperature SDE in high- $T_c$  superconductor  $\text{Bi}_2\text{Sr}_2\text{CaCu}_2\text{O}_{8+\delta}$  (BSCCO) flake devices. The nonreciprocal critical currents under zero magnetic field are observed, supporting a field-free SDE. More importantly, the operating temperature of the field-free SDE can reach 72 K and the efficiency is as high as 22% at 53 K. The rectification effect over a long-time scale further confirms the stability of the SDE. Our observation of the high-temperature field-free SDE in simple high- $T_c$  superconductor flake devices paves a way to achieve energy-efficient computation architectures and, at the time, provides valuable insights into the symmetry breakings in unconventional high- $T_c$  superconductors.

## Results

### Superconductivity of the BSCCO flake device

BSCCO is an unconventional superconductor with a high superconducting transition temperature. As shown in Fig. 1a, the high- $T_c$  superconductor BSCCO has a bilayer structure, where each layer is composed of two adjacent  $\text{CuO}_2$  planes sandwiched between BiO and SrO planes. Benefiting from the weak van der Waals interaction

between the layers, we mechanically exfoliated BSCCO flakes from BSCCO bulk samples and subsequently transferred them onto oxygen-plasma-treated  $\text{SiO}_2/\text{Si}$  substrates. Then the BSCCO flake devices were fabricated by standard electron-beam lithography technique (devices s1 and s2) and cryogenic exfoliation technique (devices s3–s8) (see more details in Methods). The optical image of a typical BSCCO flake device s1 is shown in the inset of Fig. 1b. The atomic force microscopy (AFM) measurements (Fig. 1c) reveal the thickness of device s1 is 53.5 nm (about 18 unit cells). The electrical transport properties of the BSCCO flake device were systematically studied. Figure 1b displays the temperature dependence of the resistance for device s1 at zero magnetic field from 2 to 300 K. The superconducting transition begins at the onset temperature  $T_c^{\text{onset}} = 93.6$  K, where the resistance starts to drop abruptly. The zero-resistance state is reached within the measurement resolution at  $T_c^{\text{zero}} = 75.5$  K. With increasing the perpendicular magnetic fields (applied along the  $c$ -axis), the superconductivity is suppressed and the zero-resistance state gradually vanishes (Fig. 1d). The temperature-dependent critical magnetic field  $B_c$  (defined as the field corresponding to 50% of the resistance at onset temperature) extracted from the  $R(T)$  curves shows a tail at high temperatures (Fig. 1e), which is consistent with previous studies<sup>45–47</sup> on BSCCO bulk samples.

### High-temperature field-free superconducting diode effect

We measured the voltage versus current ( $V$ - $I$ ) curves by slowly ramping the current from negative to positive (defined as positive sweep) and from positive to negative (defined as negative sweep) at various temperatures in the absence of an applied magnetic field. The  $V$ - $I$  curves at 53 K are shown in Fig. 2a. With increasing current in the positive sweep, the voltage jumps from zero to a finite value at a critical current  $I_{c+} > 0$ , corresponding to the transition to the resistive state. Reversing the current direction in the negative sweep, the voltage jump to the resistive state occurs at a critical current  $I_{c-} < 0$ . Intriguingly, despite under the zero-field condition, nonreciprocal critical currents  $|I_{c-}| \neq |I_{c+}|$  are detected. For a better comparison between the critical

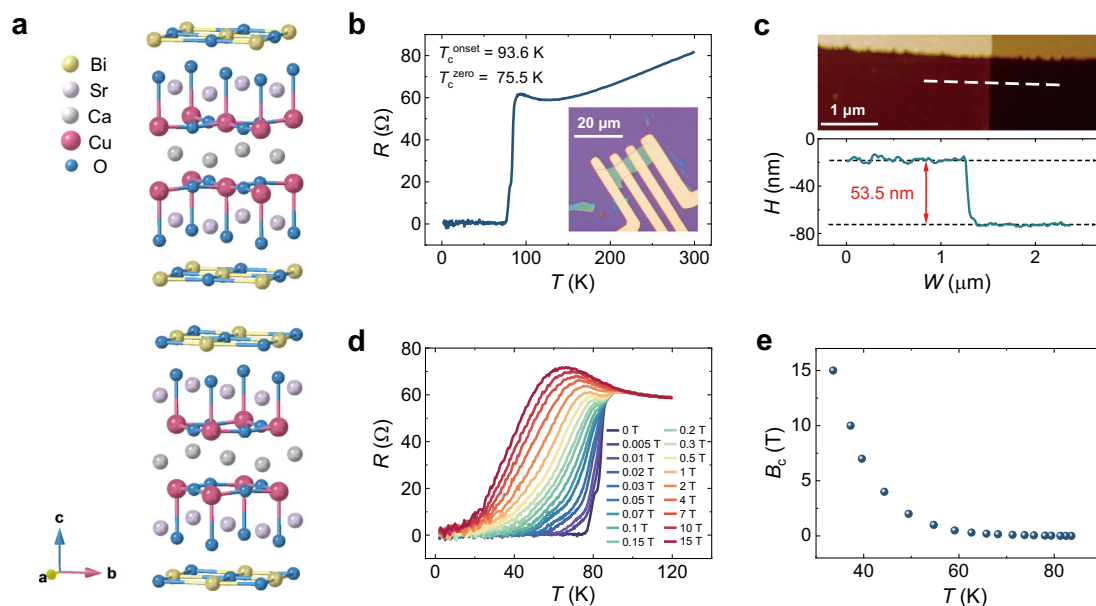


**Fig. 1 | Characterizations and superconductivity of  $\text{Bi}_2\text{Sr}_2\text{CaCu}_2\text{O}_{8+\delta}$  (BSCCO) device s1.** **a** Schematic crystal structure showing a unit-cell of the bilayer BSCCO. Each layer is composed of two conducting  $\text{CuO}_2$  planes. **b** Temperature dependence of the resistance  $R(T)$  at zero magnetic field from 2 K to 300 K. The superconducting transition temperatures  $T_c^{\text{onset}} = 93.6$  K and  $T_c^{\text{zero}} = 75.5$  K. The excitation current is 5  $\mu\text{A}$ . Inset: The optical image of the BSCCO flake device s1 on  $\text{SiO}_2/\text{Si}$  substrate with standard four-terminal electrodes. Scale bar represents 20

$\mu\text{m}$ . **c** Atomic force microscopy (AFM) topography and corresponding height profile of the BSCCO device, showing the thickness of 53.5 nm. Scale bar represents 1  $\mu\text{m}$ . The scanning direction of the height profile is along the white dashed line. **d**  $R(T)$  curves under different perpendicular magnetic fields (along the  $c$ -axis), ranging from 0 T (purple line) to 15 T (red line). **e** Temperature dependence of the perpendicular critical magnetic field  $B_c$  extracted from  $R(T)$  curves in (d).

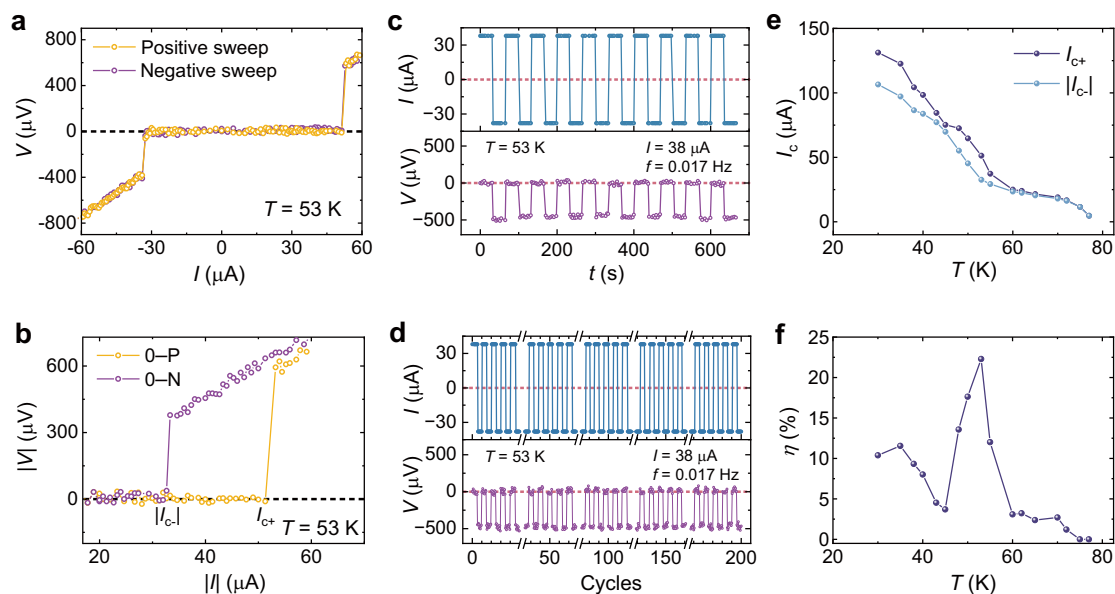


**Fig. 2 | High-temperature superconducting diode effect (SDE) at zero magnetic field in BSCCO flake device s1.** **a**  $V$ - $I$  curves measured by ramping the current from negative to positive (positive sweep, orange line) and from positive to negative (negative sweep, purple line) at 53 K. The black dashed line represents zero voltage. **b**  $V$ - $I$  curves containing O-P (sweeping from zero to positive, orange line) and O-N (sweeping from zero to negative, purple line) branches at 53 K, showing asymmetric critical current along opposite directions, namely  $I_{c+}$  and  $|I_{c-}|$ . **c** Half-wave rectification measured at 53 K under zero magnetic field, showing an alternating

switching between superconducting and resistive state depending on the direction of the current. The amplitude of the excitation current is 38  $\mu$ A and the frequency is 0.017 Hz. The red dashed lines represent the value of zero. **d** Rectification response observed in 200 cycles (over 3 h), illustrating high stability of the SDE. **e**  $I_{c+}$  and  $|I_{c-}|$  obtained from the O-P and O-N branches as a function of temperature at zero magnetic field. The diode effect vanishes at 75 K, which is very close to  $T_c^{\text{zero}}$  (75.5 K). **f** Temperature dependence of the diode efficiency  $\eta$ . The efficiency reaches its maximum around 22% at 53 K and becomes zero at 75 K.

currents in different directions, in Fig. 2b, we plot the absolute  $V$ - $I$  values in O-P (sweeping from zero to positive) and O-N (sweeping from zero to negative) branches derived from Fig. 2a. Note that the O-N branch should not be confused with a return trace, which overlaps with the O-P branch, pointing to insignificant heating effects in the resistive state. Figure 2b clearly displays a considerably larger critical current  $I_{c+}$  (51.3  $\mu$ A) than the absolute value of  $|I_{c-}|$  (32.7  $\mu$ A), suggesting the nonreciprocity of critical currents in the BSCCO flake device.

The difference of  $I_{c+}$  and  $|I_{c-}|$  indicates that if the applied current lies between  $I_{c+}$  and  $|I_{c-}|$ , the system will be in zero-resistance superconducting state for current flowing along the positive direction but in resistive state for current along the opposite direction. This is the superconducting diode effect. Considering the  $I_{c+}$  and  $|I_{c-}|$  being 51.3 and 32.7  $\mu$ A, respectively, we applied a square-wave excitation (Fig. 2c, upper panel) with an amplitude of 38  $\mu$ A at a frequency of 0.017 Hz to confirm the existence of rectification effect under zero applied magnetic field. As shown in Fig. 2c, half-wave rectification is beautifully observed as the voltage switches between zero in superconducting state and a nonzero value in the resistive state (the lower panel). The rectification effect remains stable for a series of applied current waves with different frequencies (0.007–0.033 Hz) and amplitudes (38 and 40  $\mu$ A) between  $I_{c+}$  and  $|I_{c-}|$  (Supplementary Fig. 1). The robustness of the SDE is further demonstrated by the highly stable performance of the rectification effect (Fig. 2d) over a time span of more than 3 h (200 cycles). The asymmetric  $V$ - $I$  curves and half-wave rectification effect are also observed at different temperatures. The critical currents  $I_{c+}$  and  $|I_{c-}|$  in zero applied field at various temperatures from 30 K to 77 K are plotted in Fig. 2e. As temperature increases, the superconductivity is suppressed and the absolute values of two critical currents decrease simultaneously. To quantify the strength of the diode effect, we defined the superconducting diode efficiency  $\eta = \frac{I_{c+} - |I_{c-}|}{I_{c+} + |I_{c-}|} \times 100\%$ . The diode efficiency exhibits a maximum value of

22% at 53 K and becomes zero at 75 K (Fig. 2f and Supplementary Fig. 2). The high operating temperature up to 72 K, large efficiency, zero applied magnetic field, and the simple flake configuration dramatically increase the practicability of superconducting electronic device fabricated using high- $T_c$  cuprate superconductors.

To demonstrate the field-free nature of the observed SDE, we measured  $V$ - $I$  curves at 30 K under applied perpendicular magnetic fields. The obtained critical currents  $I_{c+}$  and  $|I_{c-}|$  decrease with increasing magnitude of the magnetic field applied in both directions (Fig. 3a). For field strength below 25 mT, the measured  $I_{c+}$  is always larger than  $|I_{c-}|$ , suggesting the SDE in our BSCCO device continues to operate in weak to moderate magnetic fields. A typical  $V$ - $I$  curve of the O-P and O-N branches in a 2 mT magnetic field is displayed in Fig. 3b. The asymmetric critical current  $\Delta I_c$  ( $\Delta I_c = I_{c+} - |I_{c-}|$ ) is about 26  $\mu$ A, demonstrating the existence of the SDE. The rectification effect of the periodic switching between superconducting and resistive states is shown in Fig. 3c by changing the polarity of the applied current at an amplitude of 100  $\mu$ A and frequency of 0.017 Hz. Note that the field dependence of  $\Delta I_c$  and  $\eta$  here differs from that of the magnetic field-induced SDE, in which the  $\Delta I_c$  shows an antisymmetric field dependence<sup>31</sup>. More detailed comparison will be given in Supplementary Discussion.

The SDE is also reproducible in BSCCO flake devices s2–s8 (Figs. 4 and 5, Supplementary Figs. 3–7). Figure 4 shows a typical field-free SDE in device s8. The superconducting transition begins at  $T_c^{\text{onset}} = 98.5$  K and the zero-resistance state is reached within the measurement resolution at  $T_c^{\text{zero}} = 86.4$  K (Fig. 4a). The AFM topography (Fig. 4b) reveals the thickness of s8 is 23.8 nm (about 8 unit cells). The field-free SDE is confirmed in the  $V$ - $I$  curves containing the O-P and O-N branches in zero applied magnetic field at 60 K (Fig. 4c), which clearly display the asymmetric critical currents  $\Delta I_c$  of about 75  $\mu$ A. Figure 4d shows the temperature dependence of the diode efficiency  $\eta$ . It is also noteworthy that device s8 is fabricated by the cryogenic exfoliation technique different from that used for s1 and s2

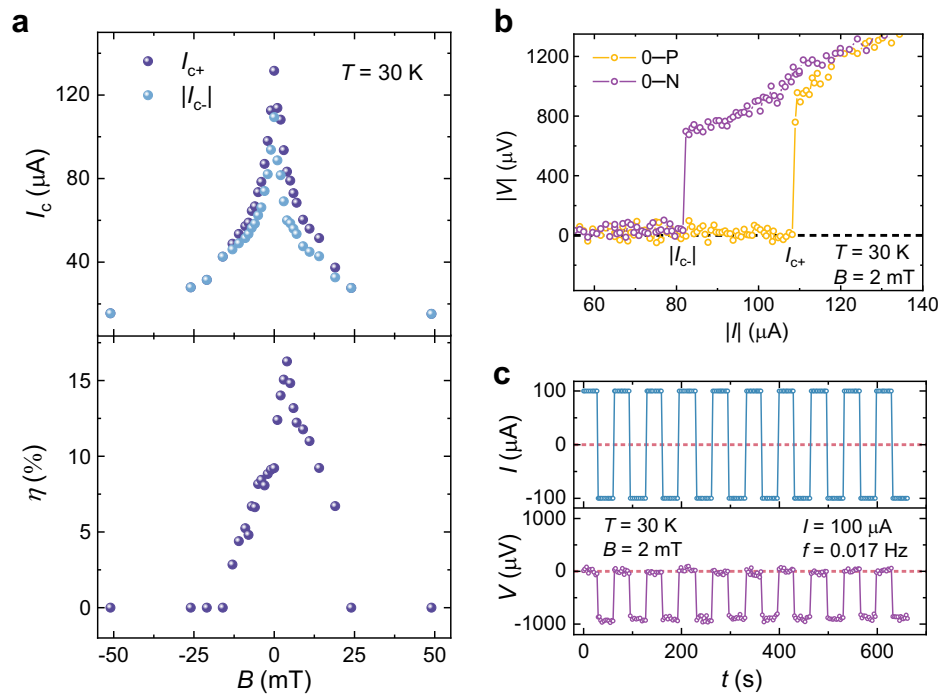


**Fig. 3 | Magnetic field dependence of the SDE in device s1. a**  $I_{c+}$  and  $|I_{c-}|$  (the upper panel) obtained from the O-P and O-N branches and the diode efficiency  $\eta$  (the lower panel) as a function of perpendicular magnetic fields at 30 K. **b** Asymmetric  $V$ - $I$  curves containing O-P (orange) and O-N (purple) branches at

30 K under perpendicular magnetic field 2 mT. The black dashed line represents zero voltage. **c** Half-wave rectification at 30 K under perpendicular magnetic field 2 mT. The amplitude of the excitation current is 100 μA and the frequency is 0.017 Hz. The red dashed lines represent the value of zero.

(see more details in Methods), indicating that the SDE in BSCCO flake devices is independent of the device fabrication techniques.

The field-free nature of the observed SDE in BSCCO flake devices is further confirmed by flipping the device in zero magnetic field. Figure 5 shows the SDE in device s6, which is installed on a rotator in measurement system. The typical SDE at 30 K, zero magnetic field, and  $0^\circ$  is shown in Fig. 5b, c. When turning the device upside down (the position of the device is changed to  $180^\circ$ , with the schematic position of the device shown in the inset of Fig. 5d), the polarity of SDE (Fig. 5d) remains the same as that in Fig. 5b, demonstrating that the SDE is not induced by the possible remanence of the superconducting magnet in the measurement system or other external magnetic field, further confirming the field-free nature of the SDE.

## Discussion

Our observation of the zero-field SDE breaks grounds for potential high operating temperature superconducting electronic applications with high efficiency using simple structures of high- $T_c$  superconductors. We next turn to discuss the plausible mechanisms for the remarkable observations. These discussions do not affect the observation of the field-free SDE in high- $T_c$  superconductors or its potential for application in superconducting electronics, and provide valuable insights into the nature of the unconventional high- $T_c$  superconducting state.

Before doing so, it is necessary to examine the role of the continuous Joule heating when applying the current in the resistive state, which may lead to the asymmetric critical currents in the  $V$ - $I$  curves<sup>34</sup>. The heating effect becomes more obvious the longer the time over which the current is driven in the resistive state. In our experiments, the  $V$ - $I$  curves are obtained from a current sweep from negative to positive and then back to negative directions. Intriguingly, the two curves, i.e., the forward and return traces, overlap with each other (Fig. 2a), which demonstrates that the Joule heating in the resistive portions of the sweeping paths is minimal and does not play a role in the nonreciprocal

critical currents. Moreover, the rectification effect remains stable over a long-time cycle (e.g., Fig. 2d), indicating that the current does not induce a significant thermal disturbance on the device, further confirming the nonreciprocal critical current is not induced by the Joule heating effect. Furthermore, we can rule out the role of asymmetric electrodes, which could lead to asymmetric  $V$ - $I$  curves not only in the superconducting region but also in the normal state of the device. We measured the  $V$ - $I$  curves of device s1 at 100 K and 120 K and device s6 at 120 K and 150 K, where the devices are in their normal state (Supplementary Fig. 8). The linear and center-symmetric curves confirm that the nonreciprocity does not originate from asymmetric electrodes. The possibility of nonreciprocity induced by artifacts of the transport experiment can also be excluded by the control experiment in conventional superconductor Nb devices using the same measurement system and cooling procedure as that used in measuring BSCCO flakes. In the Nb devices, at zero magnetic field, the O-N branch of the  $V$ - $I$  curve overlaps well with the O-P branch, pointing to  $I_{c+} = |I_{c-}|$  and the absence of zero-field SDE in Nb devices (Supplementary Figs. 9 and 10b). Under applied magnetic field, the SDE can be induced (Supplementary Fig. 10c) and the diode efficiency is antisymmetric around 0 mT (Supplementary Fig. 10d), which is a typical characteristic of the field-induced SDE and in stark contrast with the symmetric magnetic field dependence of the diode efficiency in BSCCO flakes (Figs. 3a and 5e). Therefore, the observed field-free SDE in BSCCO should be induced by the nonreciprocity of BSCCO flakes.

Generally, the emergence of the SDE requires the simultaneous breaking of time-reversal and inversion symmetries in the superconducting systems<sup>13–17</sup>. With applied external magnetic field, the SDE was observed in superconducting thin films<sup>31</sup> and artificially twisted BSCCO Josephson junctions<sup>21,22</sup>. In these experiments, the asymmetric vortex edge barriers<sup>21,31</sup>, the Meissner screening effect under the magnetic field<sup>31</sup>, and the interaction between Josephson and Abrikosov vortices<sup>22</sup> break the time-reversal and inversion symmetries and enable the SDE to be observed. However, in our experiments, the SDE was



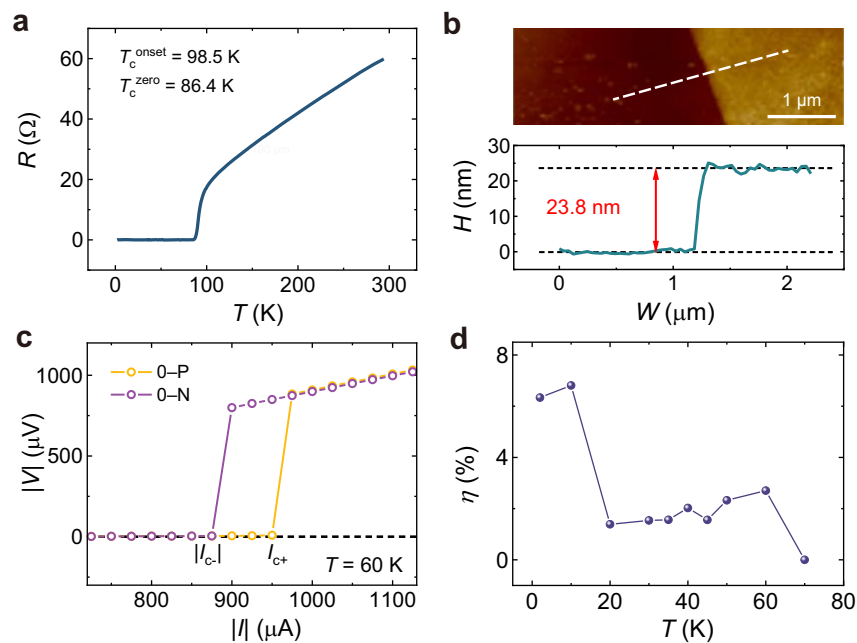


**Fig. 4 | Zero-field SDE in BSCCO flake device s8.** **a** Temperature dependence of the resistance in zero magnetic field, showing  $T_c^{\text{onset}} = 98.5$  K and  $T_c^{\text{zero}} = 86.4$  K. **b** AFM topography and corresponding height profile for device s8, showing the thickness of 23.8 nm. Scale bar represents 1  $\mu\text{m}$ . The scanning direction of the height profile is

along the white dashed line in the upper panel. **c**  $V$ - $I$  curves containing O-P (orange line) and O-N (purple line) branches at 60 K, showing nonreciprocal critical currents along opposite directions  $I_{c+} \neq |I_{c-}|$ . The black dashed line represents zero voltage. **d** Temperature dependence of the diode efficiency  $\eta$ .

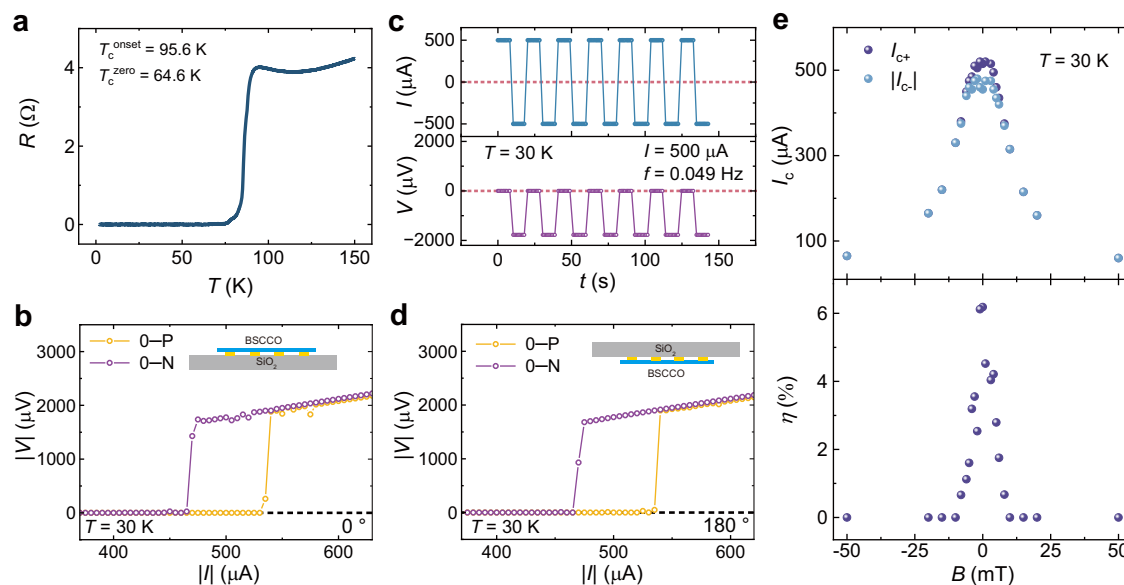


**Fig. 5 | Zero-field SDE in BSCCO flake device s6.** **a** Temperature dependence of the resistance in zero magnetic field, where  $T_c^{\text{onset}}$  is 95.6 K and  $T_c^{\text{zero}}$  is 64.6 K. The thickness of device s6 is 86.6 nm. **b**  $V$ - $I$  curves containing O-P (orange line) and O-N (purple line) branches at 30 K and  $0^\circ$ , showing nonreciprocal critical currents along opposite directions  $I_{c+} \neq |I_{c-}|$ . The black dashed line represents zero voltage. The schematic position of the device is shown in the inset. **c** Half-wave rectification measured at 30 K under zero magnetic field. The amplitude of the excitation

current is 500  $\mu\text{A}$  and the frequency is 0.049 Hz. The red dashed lines represent the value of zero. **d**  $V$ - $I$  curves containing O-P (orange line) and O-N (purple line) branches at 30 K and  $180^\circ$ , showing the same polarity of SDE as that at  $0^\circ$ , further confirming the field-free nature of the observed SDE. The inset is the schematic position of the “flipped” device. **e**  $I_{c+}$  and  $|I_{c-}|$  (the upper panel) obtained from the O-P and O-N branches and the diode efficiency  $\eta$  (the lower panel) as a function of perpendicular magnetic fields at 30 K.

observed in BSCCO flake devices without any magnetic field or magnetic layer, providing existence of a distinct mechanism for the SDE in cuprates which differs from previous studies and calls for further investigations.

If the observation of field-free SDE in BSCCO flake devices is induced by spontaneous TRS breaking, the intra-unit-cell, copper-

oxygen loop current order proposed theoretically for high- $T_c$  cuprates<sup>48–50</sup> may provide a plausible explanation. The circulating current forms below the critical temperature of the pseudogap phase, which lowers the symmetry of the crystal, leading to inversion symmetry breaking<sup>51</sup>. The loop current order is an orbital magnetic order that breaks the TRS<sup>51</sup>. The inversion symmetry and TRS breakings can

persist into the superconducting state<sup>49,52,53</sup> and produce the non-reciprocity of the critical currents in BSCCO flakes (Supplementary Discussion). The history-dependent polarity of the field-free SDE in device s7 upon thermal cycling is also consistent with this scenario (Supplementary Fig. 7 and Supplementary Discussion). Nonetheless, the detailed mechanism of the observed field-free SDE and the origin of the possible time-reversal and inversion symmetry breakings in BSCCO flakes are still widely open for future investigations. Our observation of the high-temperature SDE under zero applied magnetic field in simple BSCCO flakes breaks ground in emergent non-reciprocity of high- $T_c$  superconductors and significantly advances the feasibility and potential for non-dissipative device applications.

## Methods

### Device fabrication

The optimally doped BSCCO single crystal was purchased from PrMat. BSCCO flakes were mechanically exfoliated from the BSCCO bulk crystal using Scotch tape and transferred onto oxygen-plasma-treated SiO<sub>2</sub>/Si substrate. Then electron-beam lithography technique and cryogenic exfoliation technique were used to fabricate the BSCCO flake devices. The Nb devices composed of Nb thin film and four/six electrodes were fabricated by electron-beam lithography technique and magnetron sputtering (MSP-3200). The length, width, and thickness of the Nb film devices Nb-1 and Nb-2 between two voltage electrodes are 180  $\mu$ m, 30  $\mu$ m, and 33.8 nm, respectively. The length, width, and thickness of the Nb film device Nb-3 between two voltage electrodes are 3.6  $\mu$ m, 20  $\mu$ m, and 42.7 nm, respectively.

**The electron-beam lithography technique.** The polymethyl methacrylate (PMMA) 495 A11 was spin-coated onto the BSCCO flakes on SiO<sub>2</sub>/Si substrate. Then the electrodes were patterned through electron beam lithography in a FEI Helios NanoLab 600i Dual Beam System (Supplementary Fig. 11b). The gold electrodes (150 nm) were deposited in a LJEV-400 L E-Beam Evaporator after Ar plasma cleaning. Afterwards, the PMMA layers were removed by the standard lift-off process.

**The cryogenic exfoliation technique.** The polydimethylsiloxane (PDMS), which was prepared by mixing Sylgard 184 silicon elastomer and curing agent in a mass ratio of 10:1, and baked at 100 °C for an hour, was used to re-exfoliate the BSCCO at low temperatures. Firstly, the SiO<sub>2</sub>/Si substrate with thick BSCCO flake was put on a cold stage cooled by liquid nitrogen in an Ar-filled glove box (H<sub>2</sub>O < 0.1 ppm, O<sub>2</sub> < 0.1 ppm), and the PDMS-1 was attached to the BSCCO flake at -60 °C. As the temperature further decreased to -80 °C, the PDMS-1 was quickly pulled off to re-exfoliate the thick BSCCO flake (Supplementary Fig. 12b). Then, the BSCCO flake with the PDMS-1 was put on the cold stage and the flake was covered by another PDMS stamp (PDMS-2). Afterwards, the cold stage was cooled down to -100 °C and the PDMS-2 was quickly picked up. In this way, the BSCCO flake on PDMS-2 was completely exfoliated at low temperatures. Next, a SiO<sub>2</sub>/Si substrate with prepatterned electrodes (Ti/Au:5/30 nm) was put on the stage. The BSCCO flake on the PDMS-2 was attached to the electrodes on the SiO<sub>2</sub>/Si substrate at about -60 °C (Supplementary Fig. 12e). The PDMS-2 was slowly picked up with the temperature of the stage reaching -20 °C and the BSCCO flake devices with four-terminal electrodes were finally obtained.

### Transport measurements

Standard four-electrode method was used to characterize the transport properties of BSCCO flake devices. The transport measurements for BSCCO devices were performed using Re-liquefier based 16 T physical property measurement system (PPMS-16, Quantum Design) for devices s1, s2, and s4–s6) and cryogen-free physical property measurement system (PPMS Dynacool 9 T, Quantum Design) for devices s3, s7 and s8).

Device s6 was installed on a rotator. The d.c. mode of PPMS-16 was used to characterize the SDE in devices s1 and s5. When using d.c. mode, the applied current on the sample was automatically cut off between two adjacent voltage measurements. For the  $V$ - $I$  curves and half-wave rectification measurements of devices s2–s4 and s6–s8, a Keithley 6221 AC/DC Current Source Meter was used to apply d.c. current and square-wave excitation. The voltage was measured by a Keithley 2182A Nanovoltmeter. The transport measurements for Nb devices were performed in the same cryogen-free physical property measurement system (PPMS Dynacool 9 T, Quantum Design).

### AFM measurements

The AFM measurements of the BSCCO devices were performed in the Bruker Dimension ICON system.

### Data availability

Relevant data supporting the key findings of this study are available within the article and the Supplementary Information file. All raw data generated during the current study are available from the corresponding author upon request.

## References

- Rikken, G. L. J. A., Fölling, J. & Wyder, P. Electrical magnetochiral anisotropy. *Phys. Rev. Lett.* **87**, 236602 (2001).
- Krstić, V., Roth, S., Burghard, M., Kern, K. & Rikken, G. L. J. A. Magneto-chiral anisotropy in charge transport through single-walled carbon nanotubes. *J. Chem. Phys.* **117**, 11315–11319 (2002).
- Morimoto, T. & Nagaosa, N. Chiral anomaly and giant magnetochiral anisotropy in noncentrosymmetric Weyl semimetals. *Phys. Rev. Lett.* **117**, 146603 (2016).
- Qin, F. et al. Superconductivity in a chiral nanotube. *Nat. Commun.* **8**, 14465 (2017).
- Wakatsuki, R. et al. Nonreciprocal charge transport in non-centrosymmetric superconductors. *Sci. Adv.* **3**, e1602390 (2017).
- Neamen, D. A. *Semiconductor physics and devices: basic principles* (McGraw-Hill, 2012).
- Hu, J., Wu, C. & Dai, X. Proposed design of a Josephson diode. *Phys. Rev. Lett.* **99**, 067004 (2007).
- Ando, F. et al. Observation of superconducting diode effect. *Nature* **584**, 373–376 (2020).
- Jiang, K. & Hu, J. Superconducting diode effects. *Nat. Phys.* **18**, 1145–1146 (2022).
- Nadeem, M., Fuhrer, M. S. & Wang, X. The superconducting diode effect. *Nat. Rev. Phys.* **5**, 558–577 (2023).
- Moll, P. J. W. & Geshkenbein, V. B. Evolution of superconducting diodes. *Nat. Phys.* **19**, 1379–1380 (2023).
- Misaki, K. & Nagaosa, N. Theory of the nonreciprocal Josephson effect. *Phys. Rev. B* **103**, 245302 (2021).
- Yuan, N. F. Q. & Fu, L. Supercurrent diode effect and finite-momentum superconductors. *Proc. Natl. Acad. Sci. USA*. **119**, e2119548119 (2022).
- He, J. J., Tanaka, Y. & Nagaosa, N. A phenomenological theory of superconductor diodes. *N. J. Phys.* **24**, 053014 (2022).
- Daido, A., Ikeda, Y. & Yanase, Y. Intrinsic superconducting diode effect. *Phys. Rev. Lett.* **128**, 037001 (2022).
- Davydova, M., Prembabu, S. & Fu, L. Universal Josephson diode effect. *Sci. Adv.* **8**, eabo0309 (2022).
- Ilić, S. & Bergeret, F. S. Theory of the supercurrent diode effect in Rashba superconductors with arbitrary disorder. *Phys. Rev. Lett.* **128**, 177001 (2022).
- Pal, B. et al. Josephson diode effect from Cooper pair momentum in a topological semimetal. *Nat. Phys.* **18**, 1228–1233 (2022).
- Baumgartner, C. et al. Supercurrent rectification and magnetochiral effects in symmetric Josephson junctions. *Nat. Nanotechnol.* **17**, 39–44 (2022).

20. Turini, B. et al. Josephson diode effect in high-mobility InSb nano-flags. *Nano Lett.* **22**, 8502–8508 (2022).
21. Zhu, Y. et al. Persistent Josephson tunneling between  $\text{Bi}_2\text{Sr}_2\text{CaCu}_2\text{O}_{8+x}$  flakes twisted by  $45^\circ$  across the superconducting dome. *Phys. Rev. B* **108**, 174508 (2023).
22. Ghosh, S. et al. High-temperature Josephson diode. *Nat. Mater.* **23**, 612–618 (2024).
23. Gupta, M. et al. Gate-tunable superconducting diode effect in a three-terminal Josephson device. *Nat. Commun.* **14**, 3078 (2023).
24. Bauriedl, L. et al. Supercurrent diode effect and magnetochiral anisotropy in few-layer  $\text{NbSe}_2$ . *Nat. Commun.* **13**, 4266 (2022).
25. Yun, J. et al. Magnetic proximity-induced superconducting diode effect and infinite magnetoresistance in a van der Waals hetero-structure. *Phys. Rev. Res.* **5**, L022064 (2023).
26. Gutfreund, A. et al. Direct observation of a superconducting vortex diode. *Nat. Commun.* **14**, 1630 (2023).
27. Chen, P. et al. Edelstein effect induced superconducting diode effect in inversion symmetry breaking  $\text{MoTe}_2$  Josephson junctions. *Adv. Funct. Mater.* **34**, 2311229 (2024).
28. Sundaresh, A., Väyrynen, J. I., Lyanda-Geller, Y. & Rokhinson, L. P. Diamagnetic mechanism of critical current non-reciprocity in mul-tilayered superconductors. *Nat. Commun.* **14**, 1628 (2023).
29. Chahid, S., Teknowijoyo, S., Mowgood, I. & Gulian, A. High-frequency diode effect in superconducting  $\text{Nb}_3\text{Sn}$  microbridges. *Phys. Rev. B* **107**, 054506 (2023).
30. Lyu, Y.-Y. et al. Superconducting diode effect via confor-mal-mapped nanoholes. *Nat. Commun.* **12**, 2703 (2021).
31. Hou, Y. et al. Ubiquitous superconducting diode effect in super-conductor thin films. *Phys. Rev. Lett.* **131**, 027001 (2023).
32. Kealhofer, R., Jeong, H., Rashidi, A., Balents, L. & Stemmer, S. Anomalous superconducting diode effect in a polar super-conductor. *Phys. Rev. B* **107**, L100504 (2023).
33. Jeon, K.-R. et al. Zero-field polarity-reversible Josephson super-current diodes enabled by a proximity-magnetized Pt barrier. *Nat. Mater.* **21**, 1008–1013 (2022).
34. Wu, H. et al. The field-free Josephson diode in a van der Waals heterostructure. *Nature* **604**, 653–656 (2022).
35. Golod, T. & Krasnov, V. M. Demonstration of a superconducting diode-with-memory, operational at zero magnetic field with switchable nonreciprocity. *Nat. Commun.* **13**, 3658 (2022).
36. Narita, H. et al. Field-free superconducting diode effect in non-centrosymmetric superconductor/ferromagnet multilayers. *Nat. Nanotechnol.* **17**, 823–828 (2022).
37. Narita, H. et al. Magnetization control of zero-field intrinsic super-conducting diode effect. *Adv. Mater.* **35**, 2304083 (2023).
38. Lin, J.-X. et al. Zero-field superconducting diode effect in small-twist-angle trilayer graphene. *Nat. Phys.* **18**, 1221–1227 (2022).
39. Díez-Mérida, J. et al. Symmetry-broken Josephson junctions and superconducting diodes in magic-angle twisted bilayer graphene. *Nat. Commun.* **14**, 2396 (2023).
40. Qiu, G. et al. Emergent ferromagnetism with superconductivity in  $\text{Fe}(\text{Te},\text{Se})$  van der Waals Josephson junctions. *Nat. Commun.* **14**, 6691 (2023).
41. Zhao, S. Y. F. et al. Time-reversal symmetry breaking super-conductivity between twisted cuprate superconductors. *Science* **382**, 1422–1427 (2023).
42. Le, T. et al. Superconducting diode effect and interference patterns in kagome  $\text{CsV}_3\text{Sb}_5$ . *Nature* **630**, 64–69 (2024).
43. Scammell, H. D., Li, J. I. A. & Scheurer, M. S. Theory of zero-field superconducting diode effect in twisted trilayer graphene. *2D Mater.* **9**, 025027 (2022).
44. Hu, J.-X., Sun, Z.-T., Xie, Y.-M. & Law, K. T. Josephson diode effect induced by valley polarization in twisted bilayer graphene. *Phys. Rev. Lett.* **130**, 266003 (2023).
45. Jin, R., Schilling, A. & Ott, H. R. Temperature dependence of the magnetization of a  $\text{Bi}_2\text{Sr}_2\text{CaCu}_2\text{O}_{8+\delta}$  single crystal close to  $T_c$ . *Phys. Rev. B* **49**, 9218–9221 (1994).
46. Alexandrov, A. S., Zavaritsky, V. N., Liang, W. Y. & Nevsky, P. L. Resistive upper critical field of high- $T_c$  single crystals of  $\text{Bi}_2\text{Sr}_2\text{CaCu}_2\text{O}_8$ . *Phys. Rev. Lett.* **76**, 983–986 (1996).
47. Zavaritsky, V. N., Springford, M. & Alexandrov, A. S. c-axis negative magnetoresistance and upper critical field of  $\text{Bi}_2\text{Sr}_2\text{CaCu}_2\text{O}_8$ . *Europhys. Lett.* **51**, 334 (2000).
48. Varma, C. M. Non-Fermi-liquid states and pairing instability of a general model of copper oxide metals. *Phys. Rev. B* **55**, 14554–14580 (1997).
49. Varma, C. M. Theory of the pseudogap state of the cuprates. *Phys. Rev. B* **73**, 155113 (2006).
50. Simon, M. E. & Varma, C. M. Detection and implications of a time-reversal breaking state in underdoped cuprates. *Phys. Rev. Lett.* **89**, 247003 (2002).
51. Shekhter, A. & Varma, C. M. Considerations on the symmetry of loop order in cuprates. *Phys. Rev. B* **80**, 214501 (2009).
52. Kaminski, A. et al. Spontaneous breaking of time-reversal symmetry in the pseudogap state of a high- $T_c$  superconductor. *Nature* **416**, 610–613 (2002).
53. Leridon, B., Ng, T.-K. & Varma, C. M. Josephson effect for super-conductors lacking time-reversal and inversion symmetries. *Phys. Rev. Lett.* **99**, 027002 (2007).

## Acknowledgements

We acknowledge discussions with C. M. Varma and H. Ji, and technical assistance from R. Li, L. Pan, Y. Zhai, and S. Bai. This work was financially supported by the National Natural Science Foundation of China [Grant No. 12488201 (J.W.)], the Innovation Program for Quantum Science and Technology [2021ZD0302403 (J.W.)] and Beijing Natural Science Foundation [QY23019 (Y.A.)]. Ziqiang Wang is supported by the US Department of Energy, Basic Energy Sciences grant number DE-FG02-99ER45747.

## Author contributions

J.W. conceived and supervised the project. S.Q., J.G., C.J., Y.A., G.M., Ziqiao Wang, Z.C., and Y.L. fabricated the devices, performed the transport measurements, and analyzed the data under the guidance of J.W. Ziqiang Wang contributed to the theoretical explanations. S.Q., J.G., C.J., and J.W. wrote the manuscript with the input from Ziqiang Wang, Y.A., and Ziqiao Wang. All authors contributed the related discussions.

## Competing interests

The authors declare no competing interests.

## Additional information

**Supplementary information** The online version contains supplementary material available at <https://doi.org/10.1038/s41467-025-55880-4>.

**Correspondence** and requests for materials should be addressed to Jian Wang.

**Peer review information** *Nature Communications* thanks the anonymous reviewers for their contribution to the peer review of this work. A peer review file is available.

**Reprints and permissions information** is available at <http://www.nature.com/reprints>

**Publisher's note** Springer Nature remains neutral with regard to jurisdictional claims in published maps and institutional affiliations.

**Open Access** This article is licensed under a Creative Commons Attribution-NonCommercial-NoDerivatives 4.0 International License, which permits any non-commercial use, sharing, distribution and reproduction in any medium or format, as long as you give appropriate credit to the original author(s) and the source, provide a link to the Creative Commons licence, and indicate if you modified the licensed material. You do not have permission under this licence to share adapted material derived from this article or parts of it. The images or other third party material in this article are included in the article's Creative Commons licence, unless indicated otherwise in a credit line to the material. If material is not included in the article's Creative Commons licence and your intended use is not permitted by statutory regulation or exceeds the permitted use, you will need to obtain permission directly from the copyright holder. To view a copy of this licence, visit <http://creativecommons.org/licenses/by-nc-nd/4.0/>.

© The Author(s) 2025